Ludden, J.N., Plank, T., and Escutia, C. (Eds.)
Proceedings of the Ocean Drilling Program, Scientific Results Volume 185

9. PROGRESSIVE MICROFABRIC CHANGES IN UNCONSOLIDATED PELAGIC AND HEMIPELAGIC SEDIMENTS DOWN TO 180 MBSF, NORTHWEST PACIFIC, ODP LEG 185, SITE 1149[1]

Kiichiro Kawamura[2] and Yujiro Ogawa[3]

ABSTRACT

During Ocean Drilling Program Leg 185, we studied progressive changes of microfabrics of unconsolidated pelagic and hemipelagic sediments in Holes 1149A and 1149B in the northwest Pacific at 5818 m water depth. We paid particular attention to the early consolidation and diagenetic processes without tectonic deformation before the Pacific plate subduction at the Izu-Bonin Trench. Shape, size, and arrangement of pores were analyzed by scanning electron microscope (SEM) and were compared to anisotropy of magnetic susceptibility (AMS) data. The microfabric in Unit I is nondirectional fabric and is characterized by large peds of ~10–100 µm diameter, which are made up of clay platelets (mainly illite) and siliceous biogenic fragments. They are ovoid in shape and are mechanically packed by benthic animals. Porosity decreases from 0 to 60 meters below seafloor (mbsf) in Unit I (from 60% to 50%) in association with macropore size decreases. The microfabric of coarser grain particles other than clay in Unit II is characterized by horizontal preferred orientation because of depositional processes in Subunit IIA and burial compaction in Subunit IIB. On the other hand, small peds, which are probably made of fragments of fecal pellets and are composed of smectite and illite (3–30 µm diameter), are characterized by random orientation of clay platelets. The clay platelets in the small peds in Subunit IIA are in low-angle edge-to-face (EF) or face-to-

---

[1] Kawamura, K., and Ogawa, Y., 2002.Progressive microfabric changes in unconsolidated pelagic and hemipelagic sediments down to 180 mbsf, northwest Pacific, ODP Leg 185, Site 1149. *In* Ludden, J.N., Plank, T., and Escutia, C. (Eds.), *Proc. ODP, Sci. Results,* 185, 1–29 [Online]. Available from World Wide Web: <http://www-odp.tamu.edu/publications/185_SR/VOLUME/CHAPTERS/003.PDF>. [Cited YYYY-MM-DD]

[2] Fukada Geological Institute, Honkomagome 2-13-12, Tokyo 113-0021, Japan. kichiro@fgi.or.jp

[3] Institute of Geoscience, University of Tsukuba 1-1-1, Tennodai, Tsukuba 305-8571, Japan.

Initial receipt: 9 October 2001
Acceptance: 31 May 2002
Web publication: 16 September 2002
Ms 185SR-003

face (FF) contact. These peds are electrostatically connected by long-chained clay platelets, which are interconnected by high-angle EF contact. Breaking of these long chains by overburden pressure diminishes the macropores, and the clay platelets in the peds become FF in contact, resulting in decreases in the volume of the micropores between clay platelets. Thus, porosity in Subunits IIA and IIB decreases remarkably downward. The AMS indicates random fabric and horizontal preferred orientation fabric in Units I and II, respectively. This result corresponds to that of SEM microfabric observations.

In Subunit IIB, pressure solutions around radiolarian tests and clinoptilolite veins with normal displacement sense are seen distinctively below ~170 mbsf, probably in correspondence to the transition zone from opal-A to opal-CT.

INTRODUCTION

Argillaceous sediments change their internal microfabrics drastically at shallow burial depths by compaction resulting from particle reorientation. This process is associated with pore volume decreases (Bennett et al., 1981). The compaction model in previous studies is summarized as follows, from shallow to deep. First, clay platelets are linked by edge-to-edge (EE), edge-to-face (EF), or stepped face-to-face (FF) contact in a random arrangement, forming a long flocculation chain. This structure is called “cardhouse” fabric. Next, during further burial, such contacts in flocculations change to FF contact, forming preferred horizontal orientation (Bennett and Hulbert, 1986). These fabric changes in argillaceous sediments have been detected by shallowing of inclination of remanent magnetization, which is mostly a result of small magnetite grains of single-domain size being reoriented in preferred horizontal orientation because of compaction (Anson and Kodama, 1987; Deamer and Kodama, 1990).

At the sediment/water interface, argillaceous sediments do not have a homogeneous cardhouse fabric but have heterogeneous fabrics because of bioturbation, bottom-current disturbance, crystallization, dissolution of minerals, and so on (Reynolds and Gorsline, 1992; Bennett et al., 1991). For example, fine-grained particles are aggregated into heterogeneous fabrics by various processes as follows. Benthic animals that eat organic materials in mud make an aggregation of fine-grained particles in their own gut (Reynolds and Gorsline, 1992). Agitation by bioturbation and bottom currents at the sediment/water interface reaggregates the fine-grained particles as a result of organic matter’s adsorption and electrostatic attraction (Bennett et al., 1991; Stolzenbach et al., 1992). Then, the fine-grained particles are reoriented from EF and EE contact to FF contact by shear stress caused by the internal flow that occurs because of bioturbation and bottom-current disturbance even at the sediment/water interface. This idea was already well developed by O’Brien and Slatt (1990) and Bennett et al. (1991).

Through these complicated processes at the sediment/water interface and at shallow burial depths, fine-grained particles are eventually aggregated to what are called “peds” (Yong, 1972; Collins and McGown, 1974; Reynolds and Gorsline, 1992). Although the peds play an important role in the early compaction process of argillaceous sediments (Yong, 1972; Velde, 1996), real examples from the deep sea have not been well studied except by Collins and McGown (1974), Reynolds and Gorsline (1992), and Kawamura et al. (1999). In the present study, we will describe detailed microfabrics of the argillaceous sediments of 180-m-long cored sediments recovered from the northwest Pacific in view of peds and their interrelational development. Polarized microscope, scanning electron microscope (SEM), and magnetic fabric analyses by measuring anisotropy of magnetic susceptibility (AMS) were used for microfabric observations. Grain-size distribution and X-ray diffraction (XRD) were also conducted in this study. A new concept for the early phase of the compaction process, which gives more importance to biologic process that forms peds at various depths, is given here.

MATERIAL AND METHODS

During Ocean Drilling Program (ODP) Leg 185 at Site 1149 (Holes 1149A and 1149B), we recovered 180 m of sediments (lithologic Unit I and Subunits IIA and IIB) from the northwest Pacific, at 31°20.519′N, 143°21.078′E (Hole 1149A; 5818 m water depth) and at 31°20.532′N, 143°21.060′E (Hole 1149B; 5818 m water depth) (Fig. **F1**). Unit I (0–118.2 meters below seafloor [mbsf]) is composed of argillaceous hemipelagic sediments (late Miocene–late Pliocene in age), including many volcanic glass fragments, feldspar grains, and siliceous biogenic tests. Subunit IIA (118.2–149.5 mbsf) is characterized by brown pelagic clay, including small amounts of volcanic glass fragments and siliceous biogenic tests. Subunit IIB (149.5–180 mbsf) is composed of dominantly brown pelagic clay. The lowermost part of Subunit IIB includes zeolitic (clinoptilolite) pelagic clay below 175 mbsf. The age of Unit II is unknown because of the lack of index fossils, but comparable lithology at Deep Sea Drilling Project (DSDP) Leg 20, Hole 196 (30°1.162′N, 148°5.748′E; 6194 m water depth), ~500 km east of Site 1149, is considered to be Late Cretaceous in age (Shipboard Scientific Party, 2000). Below Subunit IIB, Cretaceous chert and marlstone continue down to ~400 mbsf, above basaltic rocks.

F1. Bathymetric map of Site 1149, p. 15.

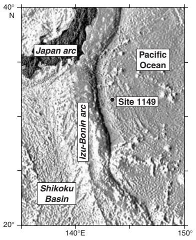

Tube samples (each ~3 cm diameter, 5 cm in length), two samples per each core, were packed on board with certain orientation in cylindric plastic cases to keep them wet until they were divided into SEM and AMS samples on shore.

Physical Properties

Since the grain density, porosity, and void ratio of Subunit IIB from Hole 1149A were not measured during Leg 185, we measured grain density (g/cm³) (ρ_g) of four samples from Subunit IIB (Samples 185-1149A-18H-2, 65–67 cm; 18H-4, 75–77 cm; 19X-1, 40–42 cm; and 20X-1, 88–90 cm) using a pycnometer. The porosity (η) and void ratio (e) were calculated from the above grain density, the water content by dry weight (W), and the dry bulk density (g/cm³) (ρ_d) reported by Shipboard Scientific Party (2000) as follows:

Void ratio in Equation (1) (Lambe and Whiteman, 1969),

$$e = \{[(1 + W)/\rho_d][\rho_g\rho_w]\} - 1, \tag{1}$$

and porosity,

$$\eta = e/(1 + e), \tag{2}$$

where ρ_w = density of seawater (typical average value) = 1.024 g/cm^3.

AMS

The AMS samples were obtained from the tube samples through the insertion of 7-cm^3 plastic cubes in the right orientations. The remains of the samples were used for smear slide observations, grain-size analysis, and XRD analysis. AMS of the cube samples was measured using a AGICO KLY-3 magnetic susceptometer at a setting of 0.04 mT low magnetic field.

The AMS is geometrically represented by a magnetic susceptibility ellipsoid with three principal axes: the maximum (K_{max}), intermediate (K_{int}), and minimum (K_{min}) magnetic susceptibility. In general, the ellipsoid is controlled by arrangement of magnetic particles in the sediments (Tarling and Hrouda, 1993). The following parameters were used in this study to represent the shape of the magnetic susceptibility ellipsoid in Equations (3) (Jelinek, 1981), (4) (Stacey et al., 1960), and (5) (Basley and Buddington, 1960):

$$P' = \exp(\mathrm{SQR}\{2[(\eta_1 - \eta m)^2 + (\eta_2 - \eta m)^2 + (\eta_3 - \eta m)^2]\}), \qquad (3)$$

$$F = K_{int}/K_{min}, \text{ and} \qquad (4)$$

$$L = K_{max}/K_{int}, \qquad (5)$$

where

η_1 = $\ln(K_{max})$;
η_2 = $\ln(K_{int})$;
η_3 = $\ln(K_{min})$,
ηm = $(\eta_1 + \eta_2 + \eta_3)/3$;
P' = corrected anisotropy degree;
F = foliation; and
L = lineation parameter.

The declinations of the K_{max}, K_{int}, and K_{min} of the AMS were corrected to magnetic north using the on board measured paleomagnetic data (Shipboard Scientific Party, 2000).

Because all the minerals in marine sediments contribute to the AMS in various degrees, it is important to define the kind of mineral most responsible for the measured magnetic fabric by the following two methods. Both vibrating sample magnetometer (VSM) measurements and SEM energy-dispersive spectrometer (EDS) analyses were used for this purpose. The VSM of Molspin Co. Ltd. measures susceptibility in high magnetic fields (K_{hf}) of 500–1000 mT. The K_{hf} is generally a result of magnetic minerals, mainly paramagnetic, not ferrimagnetic minerals (Housen and Sato, 1995; Housen, 1997). On the other hand, low field susceptibility (K_{lf}) in the sediments measured at 0.04 mT by the KLY-3 can be subdivided into components that are contributed by both ferrimagnetic and paramagnetic minerals (Housen and Sato, 1995; Housen, 1997). The ratio of K_{hf}/K_{lf} is inversely proportional to the relative contribution extent of the ferrimagnetic minerals to the K_{lf} (Housen and Sato, 1995; Housen, 1997).

Additionally, ferrimagnetic minerals were separated by a hand magnet from the sediment samples dispersed into distilled water in order to observe their individual shape. The collected ferrimagnetic minerals were attached to SEM stubs using carbon tape and then coated with carbon. Their chemical composition was analyzed using EDS.

Grain-Size Analysis

The grain-size distribution was obtained using a CIRAS1064 laser diffraction grain-size analyzer. A wet sediment weight of ~0.1 g for each sample was dispersed into boiled water in a glass beaker and then left for 24 hr than was further dispersed by an ultrasonic vibrator for 30–60 s just before measurement.

XRD Analysis

The XRD analysis was conducted for samples finer than 5 µm diameter on a polished glass slide. Three slides were analyzed for each sample in this study; the first slide sample was untreated, the next one was boiled in a dilute HCl (6 N) solution for 1 hr, and the last one was treated with ethylene glycol. CuK_{α} was used under 40-kV and 15-mA conditions by a RIGAKU RAC-A system.

Using HCl treatment, the kaolinite (001) (7 Å) peak could be identified from the original doublet peaks of kaolinite (001) and chlorite (002) because chlorite in the samples was dissolved by this treatment. Through the ethylene glycol treatment, the smectite (001) (12 Å) peak was found shifted from the original doublet peaks of chlorite (001) and smectite (001) to 15 Å. From the relative extent of each peak area, the component ratio of clay minerals was calculated in each sample qualitatively (Oinuma, 1968; Aoki and Kohyama, 1998) as follows: smectite (15 Å) = 1.0, illite (10 Å) = 3.6, chlorite (7 Å) = 3.6, and kaolinite (7 Å) = 3.6.

Preparation of Samples for SEM and Polarized Microscope

The SEM samples and thin section samples were prepared by the freeze-drying method (Takizawa et al., 1995) in order to avoid microfabric disturbance under the air-drying process that is due to the effect of surface tension of pore water. The sediment from Unit I that was subjected to the air-drying method suffered 25%–40% volume shrinkage, whereas that from Unit II suffered ~60%. As a result, the microfabrics in both units were completely distorted (Fig. F2).

F2. Comparison between freeze-drying and air-drying, p. 16.

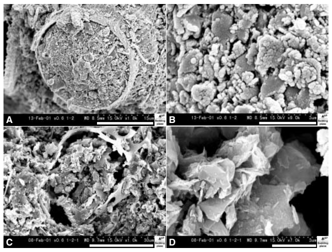

The freeze-drying method was conducted as follows. First, the pore water in the sediment was replaced by ethanol and then by *t*-butyl alcohol for several months. Next, *t*-butyl alcohol in the pores was quickly frozen by liquid nitrogen and sublimated in the vacuum desiccator. Thus, the freeze-dried samples retained the original microfabrics without any texture disruption and were best for SEM observation. The samples were coated by Au-Pd to observe the microfabrics by SEM at a setting of 15 kV and ~80 µA.

The embedded method for preparation of thin sections was conducted as follows. First, the pore water in the sediment was replaced by ethanol and then by propylene oxide for several months. Next, propylene oxide was further replaced by resin Quetol 651 from Nisshin EM Co. Ltd. Finally, the sediments were fixed under 60°C for 24 hr for thin sections.

RESULTS

Physical Properties

Grain density of four samples (185-1149A-18H-2, 65–67 cm; 18H-4, 75–77 cm; 19X-1, 40–42 cm; and 20X-1, 88–90 cm) are mostly the same, with values of 2.60, 2.60, 2.61, and 2.59 g/cm^3, respectively. The average grain density of the four samples is 2.60 g/cm^3. The porosity and void ratio calculated by this average grain density and the physical properties (Shipboard Scientific Party, 2000) are shown in Figure F3 and Table T1.

Magnetic Susceptibility and AMS

Although the magnetic susceptibility of the samples from Hole 1149A is a constant ~0.001 SI throughout Units I and II, it changes from 0.001 to 0.002 SI at three stratigraphic horizons: 120.76 mbsf (Sample 185-1149A-14H-2, 106–108 cm) in Subunit IIA, ~135 mbsf (Sample 15H-2, 116–118 cm; 130.36 mbsf, and Sample 15H-7, 36–38 cm; 137.06 mbsf) in Subunit IIB, and 170.68 mbsf (Sample 20X-1, 88–90 cm) in Subunit IIB (Fig. F3; Table T2). This change of magnetic susceptibility at these three horizons reflects the variation in content, kind, and amount of the magnetic minerals.

The magnetic minerals contributing to the magnetic susceptibility and their anisotropy are assumed to be ferrimagnetic minerals of detritic origin because of the following two reasons. The first is that the ratio of K_{hf}/K_{lf}, which reflects contribution percentage of paramagnetic minerals at low magnetic field, is <10% (Fig. F4A), suggesting that the AMS is >90% to the ferrimagnetic minerals. The second comes from a result of SEM-EDS analyses where ferrimagnetic minerals were observed as detritic shapes of ~10 µm diameter by SEM (Fig. F4B, F4C) and the chemical compositions of the minerals are predominantly O and Fe with small amounts of Ti by EDS (Fig. F4B, F4C).

The P' value <1.02 of Unit I indicates the low anisotropy degree of the magnetic susceptibility ellipsoid (Fig. F3). Although the individual ferrimagnetic mineral grains in the sediments have their own shape and AMS, the results of the AMS measurements in Unit I show low degrees of anisotropy. This means that the ferrimagnetic mineral grains probably arrange in a low degree of preferred horizontal orientation, which is mostly random in the sediment.

On the other hand, Unit II is characterized by higher P' and F values with steep K' inclination, reflecting that the ferrimagnetic mineral grains are arranged into preferred horizontal orientation (Fig. F3). The degree of the horizontal arrangement becomes more distinct from ~118 mbsf, which is the boundary between Unit I and Subunit IIA. The P' and F values in Unit II become maximum at 170.68 mbsf (Sample 185-1149A-20X-1, 88–90 cm) (Fig. F3).

The AMS of samples from Hole 1149B are characterized by low P' and F values, high L value, and low angle of K_{min} inclination (Fig. F3; Table T2). These are quite different than those from the same depths in mbsf from Hole 1149A. As the primary magnetic fabric is formed by sedimentation processes usually yielding ellipsoids with $F > L$ and K_{min} inclination >70° (Tarling and Hrouda, 1993), the results from Hole 1149B suggest that these sediments have suffered some deformation through

F3. Magnetic susceptibility, AMS, and K_{min}, p. 17.

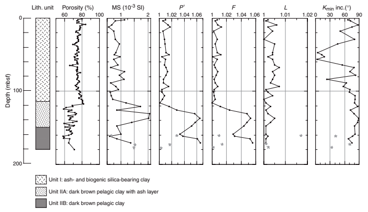

T1. Physical properties of Subunit IIB, p. 28.

T2. Magnetic susceptibility and AMS data, p. 29.

F4. Percentage of low magnetic susceptibility, p. 18.

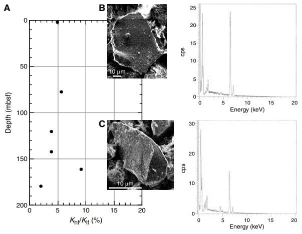

secondary effects such as bioturbation, tectonic deformation, or drilling disturbance.

Grain Size

The grain-size distribution of each sample is shown in Figure F5. The patterns in Unit I are characterized by a peak at ~10 µm diameter and a wider range in size from ~0.1 to 100 µm than that in Unit II. Some of the patterns are polymodal, having more than two peaks at ~10 µm and 25–50 µm diameter, owing to the fine particles of clay minerals and the coarse particles of volcanic glass fragments and siliceous biogenic tests.

On the other hand, the size range of Unit II is finer than that of Unit I. The grain-size distribution patterns of Subunit IIA are characterized by better sorting, with the range in size being from 0.1 to 30 µm diameter and a sharp peak of ~10 µm. Those of Subunit IIB are characterized by further finer and acuter size range from 0.1 to 25 µm and a peak of ~5 µm diameter.

The above-mentioned tendency of fining and better sorting downward may reflect a more pelagic environment in the older section.

F5. Grain-size distribution patterns, p. 19.

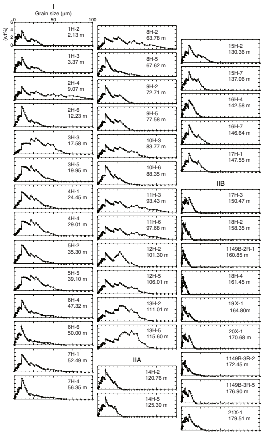

XRD Analysis

Results of the XRD analysis and clay composition are shown in Figures F6 and F7, respectively. The samples in Unit I are predominantly composed of illite, whereas those in Unit II are mainly composed of smectite and illite. Kaolinite decreases downward through Unit I to Unit II.

In the sample at 176.9 mbsf (Sample 185-1149B-3R-5, 60–62 cm), clinoptilolite (9 Å) was detected. The relative peak area of clinoptilolite (9 Å) to illite peak increases with burial depth, suggesting better crystallization in the deeper section. Opal-CT (4.04 Å) was detected in the sample at 179.51 mbsf (Sample 185-1149A-21X-1, 41–43 cm) close to the bottom of Unit II. According to correlation with results from DSDP Leg 20, Site 196, this horizon may be Cretaceous in age and corresponds to the transition zone from opal-A to opal-CT (Shipboard Scientific Party, 2000).

F6. Results of XRD, p. 20.

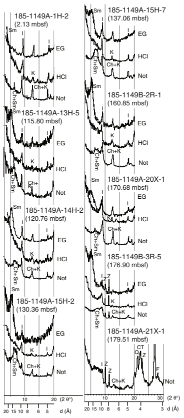

F7. Ratio of clay mineral composition, p. 21.

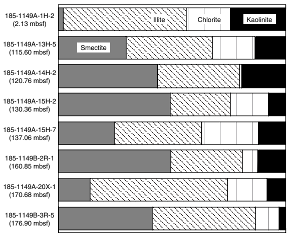

Microfabrics of Units I and II

Unit I

The microfabrics of Unit I are characterized by random arrangement of sedimentary particles (Fig. F8).

The coarse-grained particles, mainly volcanic glass fragments, are concentrated in many pipes, which are ~100 µm diameter and are considered to be burrows (Fig. F8C, F8D). The coarse-grained particles show preferred orientation along the extension direction of the pipe. As the extension direction of pipes are random in the sediment, the total orientation of the coarse-grained particles is also random.

Fine-grained particles, clay platelets, biogenic tests, and single grains are mechanically aggregated in ovoid forms of ~10–100 µm diameter as peds (Fig. F8A, F8B). Some of the biogenic tests and single grains are pressed mechanically into the ped. In the ped, some of the clay platelets are flocculated by low- to high-angle EF contact, although most of them are aggregated by low-angle EF and FF contacts. The peds are in contact with each other either directly or through bridges made of

F8. Microfabrics of Unit I, p. 22.

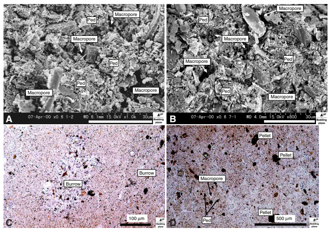

coarse-grained particles in low to high angles (Fig. F8A, F8B). The macropores at ~10–50 µm diameter could be seen between peds (Fig. F8A, F8B). The size of the macropores in the shallow depth (Sample 185-1149A-1H-2, 63–65 cm; 2.13 mbsf) is slightly larger than that in the deeper depth (Sample 7H-1, 79–81 cm; 52.49 mbsf) (Fig. F8A, F8B).

Radiolarian tests are well preserved in all microfabrics throughout Unit I, but there are different types between the inside and outside of the burrow. Inside the burrow, many radiolarian tests are filled with fine sediments (Figs. F2B, F8C), whereas those outside the burrows are vacant (Fig. F8C). This suggests that the radiolarian tests filled their own inside pore spaces with fine sediments as a result of activities of benthic animals during burrowing.

Unit II

The microfabrics are characterized by dimensional preferred horizontal orientation of coarse-grained particles of ~10–100 µm length (Figs. F9C, F10B, F10C, F10D), although the compositions of coarse-grained particles are different in Subunits IIA and IIB. In Subunit IIA, such coarse-grained particles, mainly quartz and feldspar, form thin layers of ~0.5–1.0 mm thickness at sporadic depths (Fig. F9D). These laminations may result from episodic pulses of low density, low-velocity turbidity currents, and/or of volcanic ash falling. High *P′* and *F* values in Subunit IIA probably result from these laminations. On the other hand, the coarse-grained particles in Subunit IIB are mainly composed of fragments of biogenic tests and fecal pellets showing preferred horizontal orientation (Fig. F10B, F10D) formed in association with mechanical compaction by overburden pressure.

F9. Microfabrics of Subunit IIA, p. 23.

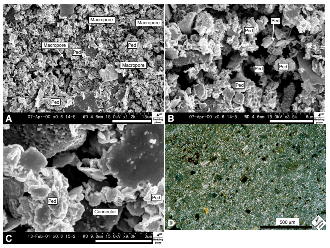

F10. Microfabrics of Subunit IIB, p. 24.

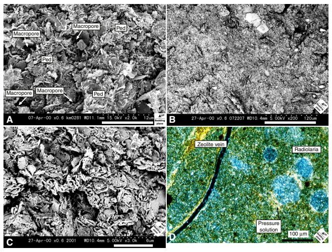

Although the grains of preferred horizontal orientation obtained from AMS analysis in Subunits IIA and IIB are consistent with the orientation of the coarse-grained particles, the fine-grained particles show random fabric under high-magnification SEM (Figs. F9A, F9B, F10A, F10C). At 125.30 mbsf (Sample 185-1149A-14H-5, 110–112 cm) and 125.30 mbsf (Sample 14H-5, 110–112 cm) of Subunit IIA, clay platelets (mainly smectite and illite) contact at low angle in EF and FF fashion. Those clay platelets are aggregated to small spheres of ~3–30 µm diameter as peds (Fig. F9A, F9B). The small peds are connected by long chains of clay platelets at high-angle EF contact (Fig. F9C). Many macropores of ~5–10 µm diameter are present between the small peds behind the long connectors so that the microfabrics in Subunit IIA are porous.

On the other hand, the boundary of the small peds is unclear at 150.47 mbsf (Sample 185-1149A-17H-3, 77–79 cm), 164.8 mbsf (Sample 19X-1, 40–42 cm), and 170.68 mbsf (Sample 20X-1, 88–90 cm) of Subunit IIB (Fig. F10A). Elongated small peds of wedge shape are aligned along the bedding plane. The microfabrics are in direct contact with each other (Fig. F10A). Therefore, some of the sediments in Subunit IIB are not porous. In the small ped, several clay platelets contact in FF to form small units as paper-stacking structure at a smaller scale (10 µm) (Fig. F10A, F10C). The orientation of small units is random in the ped a mosaic fabric in larger scale (100 m) (Fig. F10B, F10C).

F11. Palynomorphs, vertical views, p. 25.

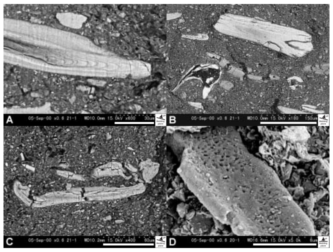

Palynomorphs are seen at 170.68 mbsf (Sample 185-1149A-20X-1, 88–90 cm) and 179.51 mbsf (Sample 21X-1, 41–43 cm), the bottom of Subunit IIB (Fig. F11). There is a growth ring as an internal microstructure (Figs. F10B, F11A), and the surface microstructure is composed of many micropores (Fig. F11D). Some of the palynomorphs are in a closed ellipsoidal form with a long axis parallel to the bedding plane

(Fig. F11C). Because their original shapes are commonly spherical (O'Brien and Slatt, 1990), these ellipsoidal forms indicate the minimum amount of compaction that took place during burial. This further supports the assumption that this initially flocculated sediment has suffered vertical flattening and transformed to shale as explained by O'Brien and Slatt (1990).

The radiolarian tests in Subunit IIB are quite different in the degree of preservation from those in Unit I and Subunit IIA, although the latter are not well preserved. Those in Subunit IIB are not only poorly preserved but are also recrystallized by diagenesis, as marked by opal-CT fillings detected by XRD analysis (Fig. F10D). Furthermore, under the polarized microscope, the bright area surrounding the radiolarian tests can be recognized as pressure solution (Fig. F10D). The degree of brightness and width of the pressure solution increase with burial depth. Platy microcrystals are seen in the pressure solution under high magnification (1000×). The shape, optical properties, and XRD analysis of the platy grains indicate that they are clinoptilolite.

These platy microcrystals (clinoptilolite) of 10–50 µm in length are also observed in veins at 164.85 mbsf (Sample 185-1149A-19X-1, 40–42 cm), 170.68 mbsf (Sample 20X-1, 88–90 cm), and 179.51 mbsf (Sample 21X-1, 41–43 cm), Subunit IIB (Fig. F12A, F12B, F12C). The veins are recognized in two directions as a conjugate set that inclines ~45° against the bedding plane (Fig. F12A). Most of the veins cut laminations with a normal sense of displacement (Fig. F12A), and they are further cut by other larger normal faults (Fig. F12A).

F12. Microfabrics of Subunit IIB, p. 26.

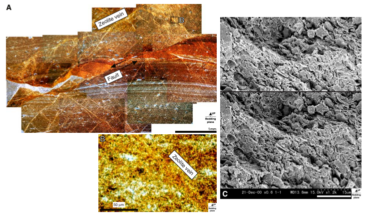

Based on the above results, a schematic model of the microfabrics in Units I and II is illustrated in Figure F13.

DISCUSSION

The peds in Unit I are relatively large in size (10–100 µm diameter), with porous fabric, and are composed of several kinds of particles. In contrast, those in Unit II are small-sized clay aggregations (3–30 µm diameter). The different features and scales of peds at different depths provide different formation processes, as discussed below.

F13. Schematic model of microfabrics, p. 27.

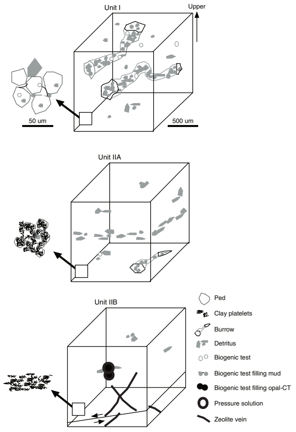

How fine sediment is aggregated into a flocculated domain to form a ped plays an important role in the pore distribution and framework of the microfabric. Three characteristics, the mode of arrangement of particles, the shape and size of peds and pores, and the degree of recrystallization of minerals, systematically change downward. Together with these changes, many physical properties also change continuously downward. These relations are discussed below with the progressive compaction process.

Origin of Large Peds in Unit I

The formation processes of microfabric in argillaceous sediments through deposition to burial are physical-chemical, bioorganic, and burial diagenesis as discussed by Bennett et al. (1991). According to them, the physical-chemical processes, including bonding mechanisms by van der Waal's attraction, electrostatic attraction, and heating effects, play a major role in microfabric development during the fluvial and eolian transport stage of particulates and on their contact with a depositional interface. The bioorganic process plays an important role in marine and coastal environments during transport and sedimentation of particulates, particularly in surficial sediments. It includes three biotic mechanisms. First is a biomechanical mechanism, which is the aggregation and disturbance of particulates by planktonic and benthic animals. For example, burrow and fecal pellets are produced by this mechanism. Second is the biophysical mechanism, in which each particulate is flocculated by organic materials as marine snow. Third are the biochemical mechanisms, in which authigenic minerals are formed by bacterial activities in sediment as a formation process of framboidal pyrite. The processes of burial diagenesis drives microfabric development when overburden or tectonic stresses dominate physical-chemical and bioorganic bonding energies (Bennett et al., 1991). In Unit I, because the original sedimentary fabrics (e.g., volcanic ash layer) are completely disturbed by bioturbation, the microfabric is affected by the bioorganic mechanism, especially biomechanical processes but not by physical-chemical mechanism.

Several studies of the microfabric of Holocene sediments have been published on micrographs of features similar to the large peds described in this study. For example, Collins and McGown (1974) described regular aggregations from several kinds of marine sediments similar to the large peds. However, they used an air-drying technique that might have changed the original texture of some artifacts; exact correlation of internal microfabrics between the regular aggregation of these studies and large peds in this study is difficult. Reynolds and Gorsline (1992) observed biofloc from hemipelagic clayey sediments (Santa Monica Basin off the California coast) whose structure is similar to the large peds described in this study. The bioflocs were observed only in the sediments and rocks with bioturbation but were not observed in nonbioturbated turbidite mud and mudstone deposited under anoxic conditions. They concluded that the origin of bioflocs is due to dissolution of fecal pellets and/or pellets of benthic animals because the bioflocs could not be observed in sediments that are not affected by biomechanical processes. Therefore, it is believed that the present peds and their aggregation are the result of biomechanical processes working in pellet formation.

The large peds in Unit I are mechanically compressed in an ovoid shape at a shallower depth than 2.13 mbsf (Sample 185-1149A-1H-2, 63–65 cm). The possible mechanism of mechanical compression in such shallow burial depth is the aggregation process by benthic animals as biofloc. The large peds are clearly distinguished from the fecal pellets in texture and color by polarized microscope observations. Fecal pellets are clearer in shape and darker than peds (Fig. F8D). This confirms our conclusion that the origin of large peds is pellets of benthic animals.

Origin of Connector and Small Peds in Unit II

The connectors are long chains of clay platelets in EF contact. In the Mississippi Delta, sediments are dominated by domains of low- to high-angle EF contacts because of physical-chemical flocs (Bennett et al., 1981). The physical-chemical process in marine sediment is due to electrostatic attraction between clay platelets. EF-particle contacts dominate because the faces of clay minerals are negatively charged, whereas the edges are positively charged (Bennett and Hulbert, 1986). In general, the clay platelets at EF contacts form long chains at shallow burial depths as cardhouse fabric (Bennett et al., 1981). Therefore, the connectors in Subunit IIA are probably formed by electrostatic attraction in shallow burial depths and are preserved at the present depths.

The small peds of clay platelets at low-angle EF and FF contacts observed in this study are similar to floc described in some pelagic clays at 143 mbsf in the eastern equatorial Pacific (Bennett et al., 1981). The outer boundaries of the flocs are well defined, and their structure in transmission electron microscope images is not similar to physical-chemical flocs (Reynolds and Gorsline, 1992). Throughout deposition and burial, there are many possible processes that clay platelets are formed from low-angle EF and FF contact (Bennett et al., 1991). For example, FF contacts are constructed either by the burial compaction process of flocculated clay platelets of EF contacts (Bennett et al., 1981, 1991) or by dispersion depositional process that lack strong bonding (e.g., electrostatic attraction) at each contact point of the clay platelets (Moon and Hurst, 1984; Bennett et al., 1991).

Another mechanism of clay platelets at low-angle EF and FF contacts is clay aggregation processes by zooplankton, which produces a fecal pellet of ~100 µm diameter (Bennett et al., 1991). Small peds could form through fragmentation of such fecal pellets. Pellets of zooplankton play an important role in transporting clay platelets from the sea surface to the seabed under pelagic environments (Honjo, 1978). During sinking in seawater, they become porous and fragile because much of the organic matter (5.6–18 wt%) (Honjo, 1978) in the pellet is decomposed by bacterial activity (Honjo and Roman, 1978). In sediment-trap studies, fragmental pellets of several tens of micronmeters diameter have been described (Honjo, 1978, 1979). Some of the fragmental pellets probably further become porous and fragile by decomposition of calcareous and siliceous biogenic tests, whose contents are 10%–50% and <5%, respectively. Residue of pellets after such decomposition preserves biomechanical aggregation of clay platelets, and it is further dispersed by shear stress because of the internal flow by bioturbation and bottom-current disturbance. These fragmental fecal pellets are still connected by long chains of clay platelets in EF contact as a result of electrostatic attraction as small peds, which we saw in our samples in Subunit IIA.

Compaction Process of Units I and II

The porosity decreases steadily down to ~60 mbsf but increases to 118 mbsf at the boundary between Units I and II and then decreases steadily again down to 180 mbsf at the boundary between Units II and III. The decrease in rate from 0 to 60 mbsf and that from 118 to 180 mbsf is different, indicating different compaction processes.

In Unit I, porosity decreases from ~70% to 60% down to 60 mbsf. Magnetic fabric reflects random orientation of magnetic minerals in Unit I (Fig. F3). The size and shape of the large peds do not change with depth (Fig. F8A, F8B). In between the large peds, however, the contact of each coarse-grained particle changes from a high-angle EF contact to low-angle EF and FF contact compaction (Fig. F8). Coarse-grained particles would slide and rotate perpendicular to the maximum effective stress direction. Even through such particle rearrangement, the total direction of the particle keeps random arrangement. The size and shape of the large ped do not change during compaction. Thus, the macropores would reduce their size during early compaction in Unit I, resulting in porosity decreases in Unit I.

In Unit II, the porosity decreases from ~60% to 50% by overburden pressure are probably due to connector breakage and small ped deformation. Subunit IIA still has distinctive connectors that interconnect the small peds, whereas they are unclear in Subunit IIB (Figs. F8, F9). The connector represents a concentration point of the effective stress in the microfabrics. As the effective stress works at the connecting edge between the peds, compaction is expected to be present by deformation and destruction of connectors, as shown by Griffiths and Joshi (1990). As a result, the macropores between the small peds would close with this connector breakage process. After the connectors are broken completely, the vertical effective stress induces the changes of shape of the small peds (Fig. F13). The contact of clay platelets in the small ped also changes from EF to FF (Fig. F9). Micropores between the clay platelets in EF contact are reduced during ped deformation in accordance with the porosity decrease. These processes would contribute to porosity decrease in Unit II.

ACKNOWLEDGMENTS

This research used samples and/or data provided by the Ocean Drilling Program (ODP). ODP is sponsored by the U.S. National Science Foundation (NSF) and participating countries under management of Joint Oceanographic Institutions (JOI), Inc. This work was supported in part by a Grant-in-Aid from the Ministry of Education, Culture, and Sports, Japan (A-10304037).

The authors gratefully acknowledge Dr. A.L. Abdeldayem (Tanta University) for carefully reading the manuscript and Dr. T. Yamazaki and Dr. H. Oda (Advanced Industry of Science and Technology) for the help in AMS and the VSM measurements. Also, thanks go to Dr. K. Ikehara (Advanced Industry of Science and Technology) for measurements of the grain size distribution, Dr. T. Takeda (Kyushu University) for many comments on the magnetic properties, and Dr. T. Itabashi (OYO Co. Ltd.) for measurement of the grain density. Dr. T. Sato (Fukada Geological Institute), who kindly revised an early version of the manuscript, is greatly appreciated.

References

Aoki, S., and Kohyama, N., 1998. Cenozoic sedimentation and clay mineralogy in the northern part of the Magellan Trough, Central Pacific Basin. *Mar. Geol.,* 148:21–37.

Anson, G.L., and Kodama, K.P., 1987. Compaction-induced shallowing of the post-depositional remanent magnetization in a synthetic sediment. *Geophys. J. R. Astron. Soc.,* 88:673–692.

Bennett, R.H., Bryant, W.R., and Keller, G.H., 1981. Clay fabric of selected submarine sediments: fundamental properties and models. *J. Sediment. Petrol.,* 51:217–232.

Bennett, R.H., and Hulbert, M.H., 1986. *Clay Microstructure:* Boston (International Human Resources Development Corp. Publ.).

Bennett, R.H., O'Brien, N.R., and Hulbert, M.H., 1991. Determinants of clay and shale microfabric signatures: processes and mechanisms. *In* Bennett, R.H., Bryant, W.R., and Hulbert, M.H. (Eds.), *Microstructure of Fine-Grained Sediments: From Mud to Shale:* New York (Springer-Verlag), 5–32.

Collins, K., and McGown, A., 1974. The form and function of microfabrics features in a variety of natural soils. *Geotech.,* 24:223–254.

Deamer, G.A., and Kodama, K.P., 1990. Compaction-induced inclination shallowing in synthetic and natural clay-rich sediments. *J. Geophys. Res.,* 95:4511–4530.

Griffiths, F.J., and Joshi, R.C., 1990. Clay fabric response to consolidation. *Appl. Clay Sci.,* 5:37–66.

Honjo, S., 1978. Sedimentation of materials in the Sargasso Sea at a 5367 m deep station. *J. Mar. Res.,* 36:469–492.

————, 1979. Material fluxes and modes of sedimentation in the mesopelagic and bathypelagic zones. *J. Mar. Res.,* 38:53–97.

Honjo, S., and Roman, M.R., 1978. Marine copepod fecal pellets: production, preservation and sedimentation. *J. Mar. Res.,* 36:45–57.

Housen, B.A., 1997. Magnetic anisotropy of Barbados prism sediments., *In* Shipley, T.H., Ogawa, Y., Blum, P., and Bahr, J.M. (Eds.), *Proc. ODP, Sci. Results.,* 156: College Station TX (Ocean Drilling Program), 97–105.

Housen, B.A., and Sato, T., 1995. Magnetic anisotropy fabrics from the Cascadia accretionary prism. *In* Carson, B., Westbrook, G.K., Musgrave, R.J., and Suess, E. (Eds.), *Proc. ODP, Sci. Results,* 146 (Pt 1): College Station, TX (Ocean Drilling Program), 233–254.

Jelinek, V., 1981. Characterization of the magnetic fabric of rocks. *Tectonophysics,* 79:63–67.

Kawamura, K., Ikehara, K., Kanamatsu, T., Fujioka, K., and Ogawa, Y. 1999. Compaction process of Pelagic clay from Parece Vera Basin. *In* Saito, Y., Ikehara, K., and Katayama, H. (Eds.), *Proc. Int. Workshop on Sediment Transport and Storage in Coastal Sea-Ocean System:* Tsukuba, Japan, 441–446.

Lambe, T.W., and Whitman, R.V., 1969. *Soil Mechanics:* New York (Wiley).

Moon, C.F., and Hurst, C.W., 1984. Fabrics of muds and shales: an overview. *In* Stow, D.A.V., and Piper, D.J.W. (Eds.), *Fine-Grained Sediments: Deep-Water Processes and Facies.* Spec. Publ.—Geol. Soc. London, 15:579–593.

O'Brien, N.R., and Slatt, R.M. 1990. *Argillaceous Rock Atlas:* New York (Springer-Verlag).

Oinuma, K., 1968. Method of quantitative estimation of clay minerals in sediments by X-ray diffraction analysis. *J. Toyo Univ. Nat. Sci.,* 10:1–15.

Reynolds, S., and Gorsline, D.S., 1992. Clay microfabrics of deep sea mud(stones), California Continental Borderland. *J. Sediment. Petrol.,* 62:41–53.

Shipboard Scientific Party, 2000. Leg 185 summary: inputs to the Izu-Mariana subduction system. *In* Plank, T., Ludden, J.N., Escutia, C., et al., *Proc. ODP, Init. Repts.,* 185: College Station TX (Ocean Drilling Program), 1–63.

Stacey, F.D., Joplin, G., and Lindsay, J., 1960. Magnetic anisotropy and fabric of some foliated rocks from S.E. Australia. *Geofis. Pura Appl.,* 47:30–40.

Stolzenbach, K.D., Newman, K.A., and Wong, C.S., 1992. Aggregation of fine particles at the sediment-water interface. *J. Geophys. Res.,* 97:17889–17898.

Takizawa, S., Kawata, T., and Ohono, Y., 1995. A method of fixation and freeze drying of soft sediments containing water. *Chishitsugaku Zasshi,* 101:941–944.

Tarling, D.H., and Hrouda, F., 1993. *The Magnetic Anisotropy of Rocks:* London (Chapman and Hall).

Velde, B., 1996. Compaction trends of clay-rich deep sea sediments. *Mar. Geol.,* 133:193–201.

Yong, R.N., 1972. Soil technology and stabilization. *Proc. 4th Asia Regional Conference on Soil Mechanics and Foundation Engineering,* 2:111–124.

Figure F1. Bathymetric map of Site 1149 study area.

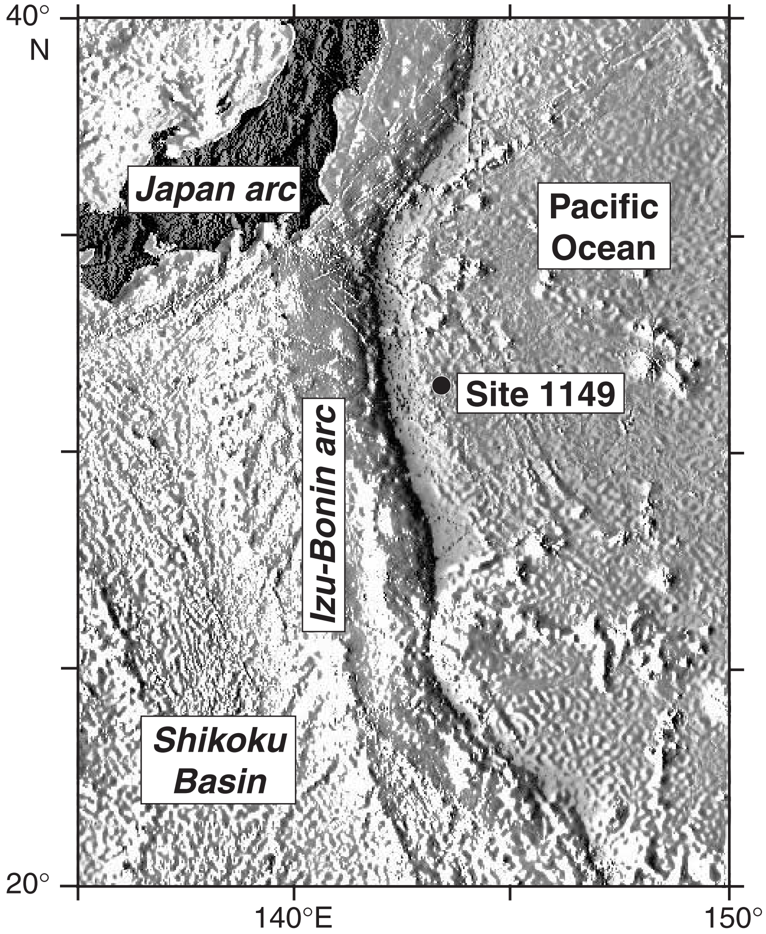

Figure F2. Comparison between both microfabrics treated by the freeze-drying and air-drying methods. Vertical views, secondary electron images at 2.13 mbsf (Sample 185-1149A-1H-2, 63–65 cm), Unit I. **A.** Microfabric treated by freeze-drying method. Note that fine sediments fill in radiolarian test. **B.** Close-up image of center of A. Clay platelets have EF contact. **C.** Microfabric treated by air-drying method, 60 oc, 24 hr. Volume shrinkage of sediment is 40.53%. Length shrinkage of sediment is 15.08% (vertical direction), 16.03% (lateral direction), and 16.60% (depth direction) in this micrograph. **D.** Close-up image of center of C. Most of clay platelets are in low-angle EF and FF contact.

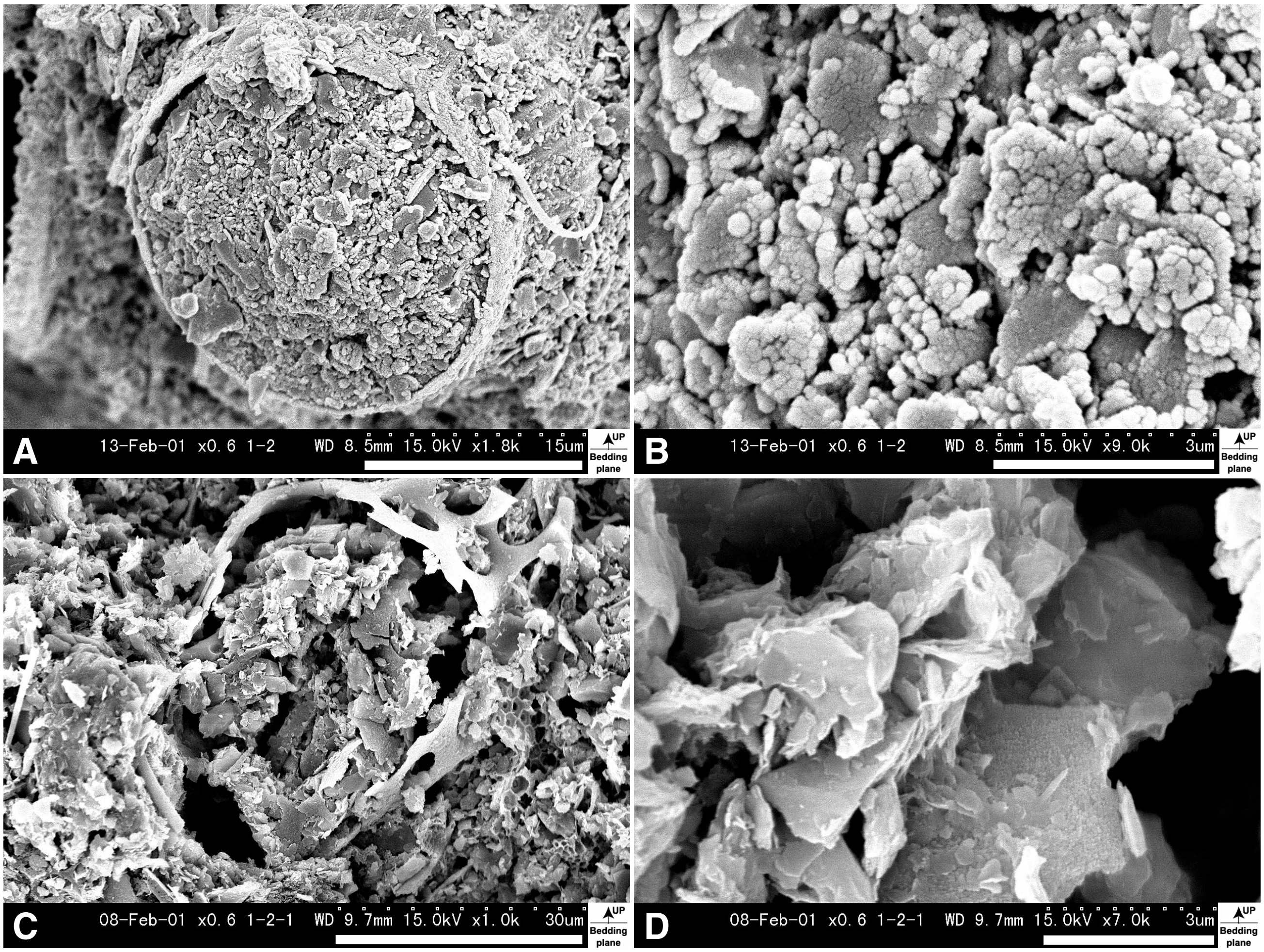

Figure F3. Profiles of magnetic susceptibility (MS), AMS parameters, and K_{min} inclination with depth. Dots and solid lines show data from Hole 1149A, and gray stars show data from Hole 1149B. From left side of figure, magnetic susceptibility profile, P' value (anisotropy degree of MS) profile, F value (foliation degree) profile, L value (lineation degree) profile, and K_{min} (minimum direction of MS) inclination profile.

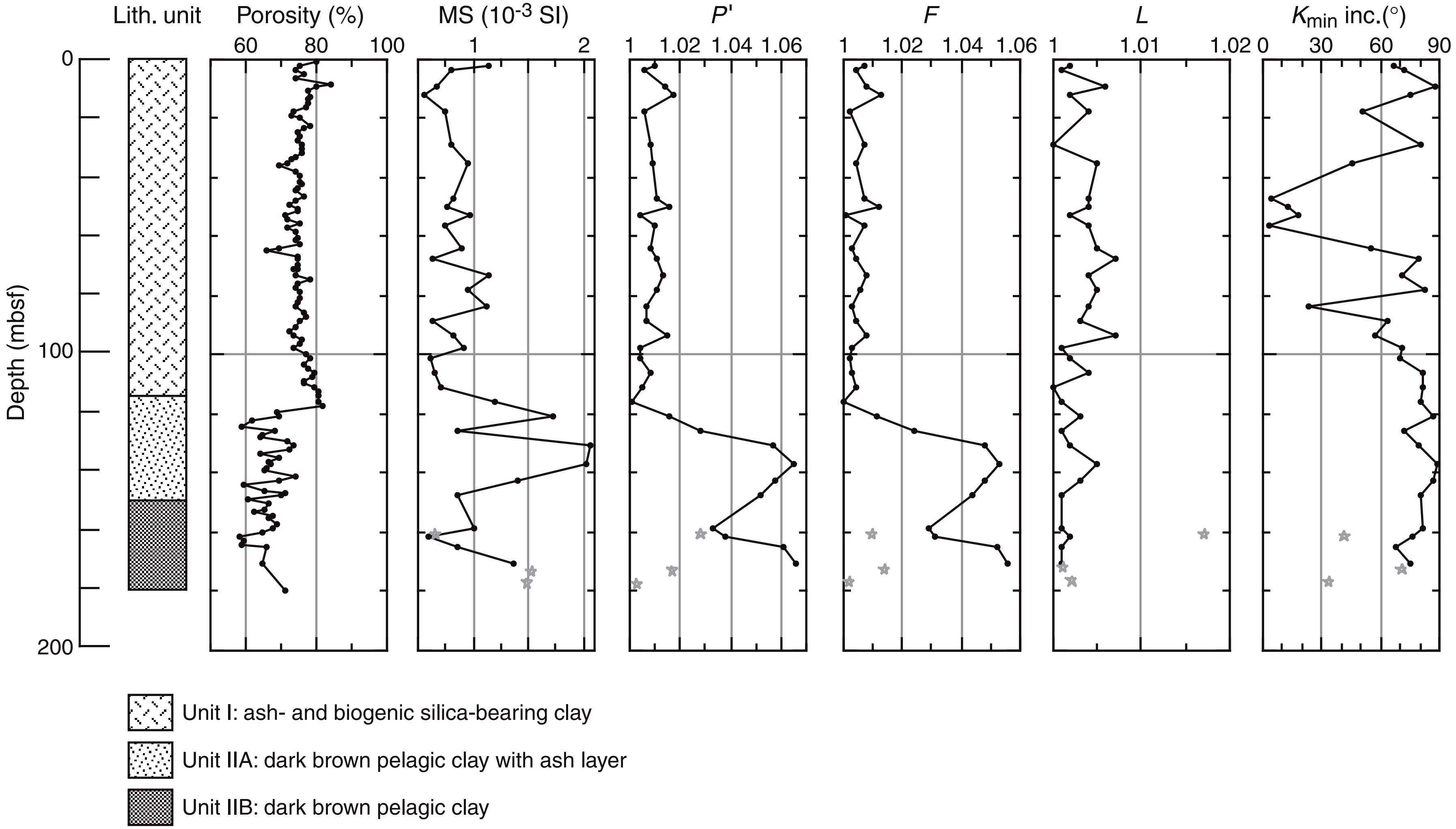

Figure F4. **A.** Depth vs. percentage of low magnetic susceptibility (K_{lf}) carried by paramagnetic minerals in sediments from Hole 1174B, as determined by comparing high-field and low-field susceptibilities. The majority (>90%) of K_{lf} is carried by ferrimagnetic minerals. **B.** Individual shape of detrital ferrimagnetic mineral grains (left) and its element composition (right) in Unit I. **C.** Individual shape of detrital ferrimagnetic mineral grains (left) and its element composition (right) in Unit II. K_{hf} = high magnetic fields, keV = kiloelectron volt.

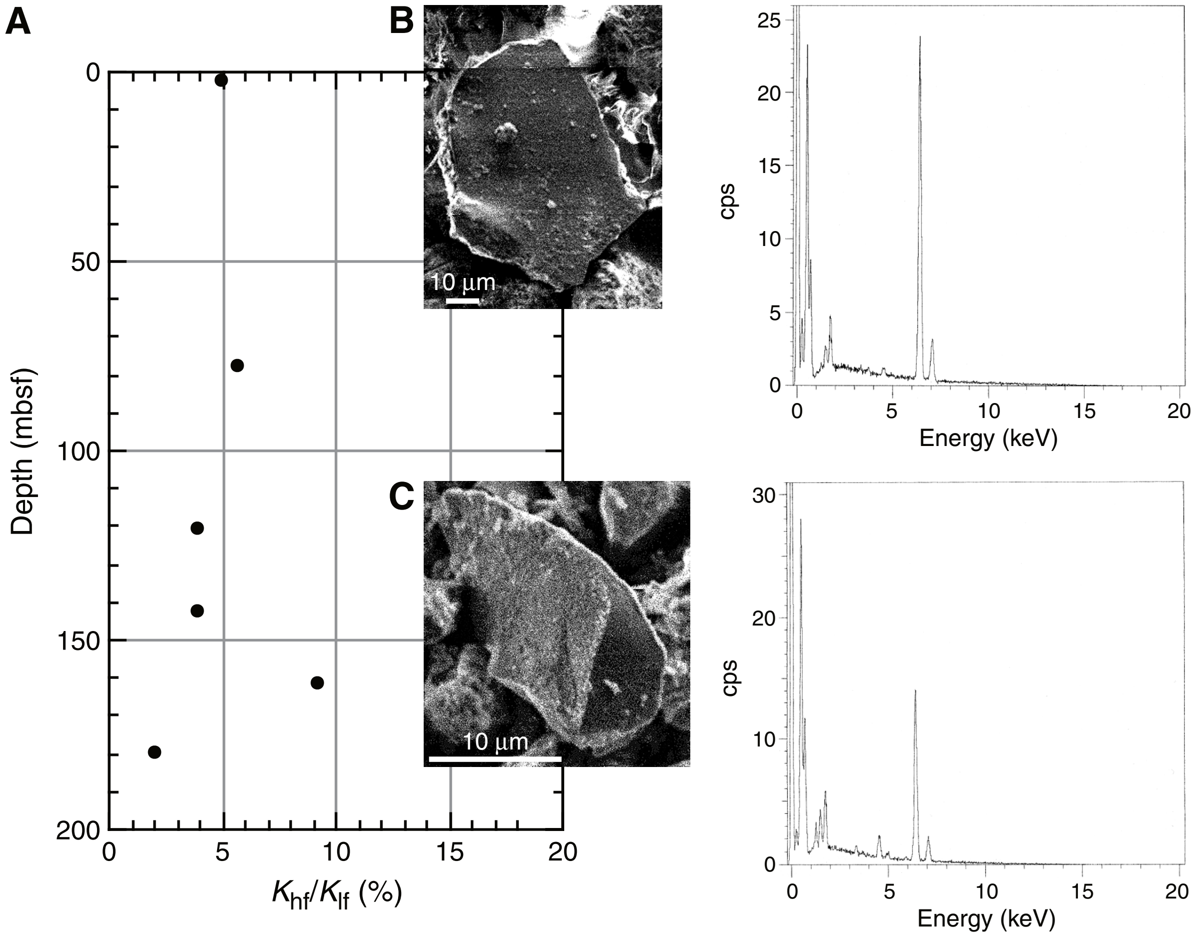

Figure F5. Grain-size distribution patterns from Unit I and Subunits IIA and IIB.

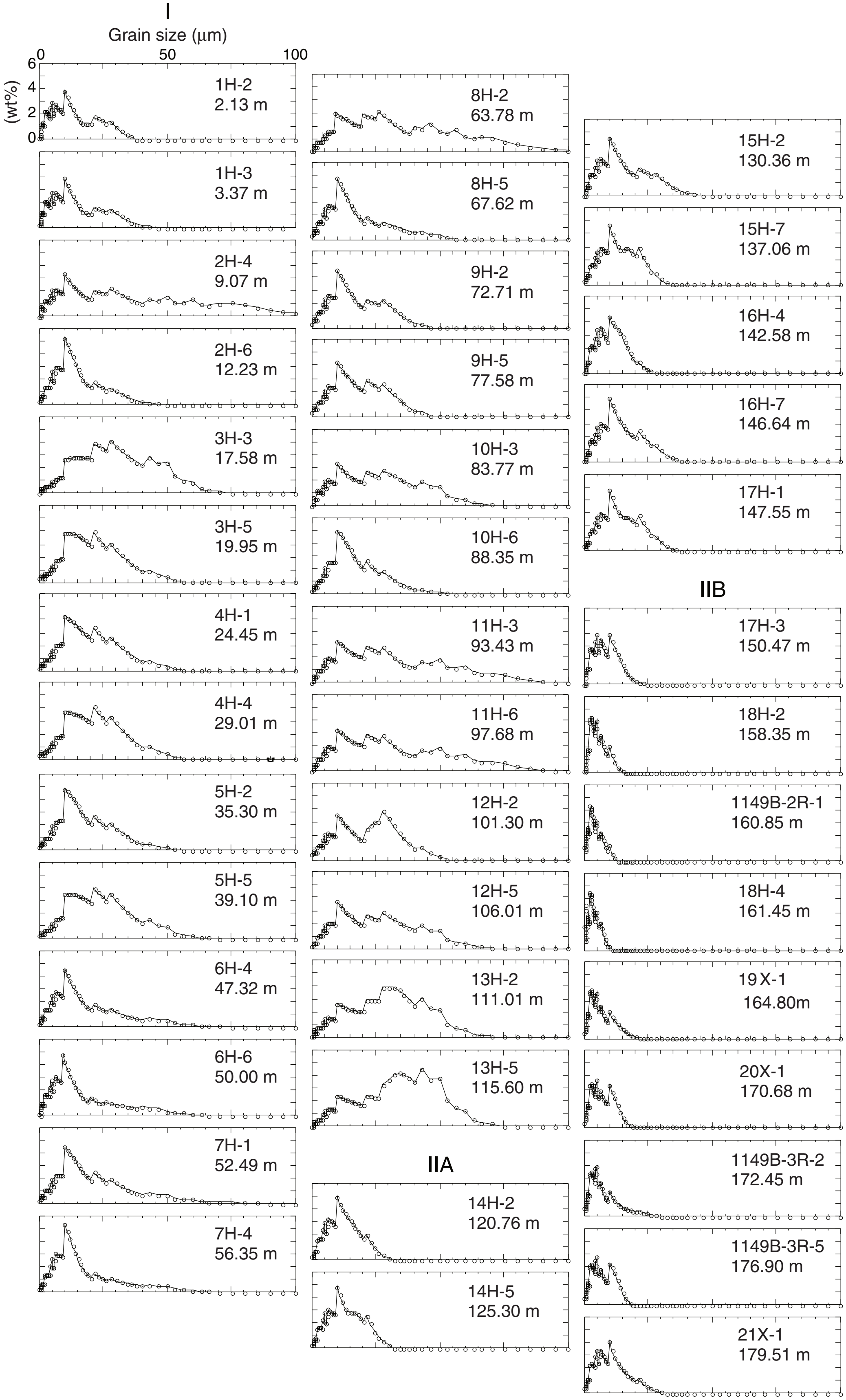

Figure F6. Results of XRD. Peaks represent smectite (Sm), illite (I), chlorite (Ch), kaolinite (K), quartz (Q), feldspar (F), zeolite (Z), and opal-CT (CT). EG = sample treated by ethylene glycol. HCl = sample treated by HCl. Not = sample not treated. d = d-spacing.

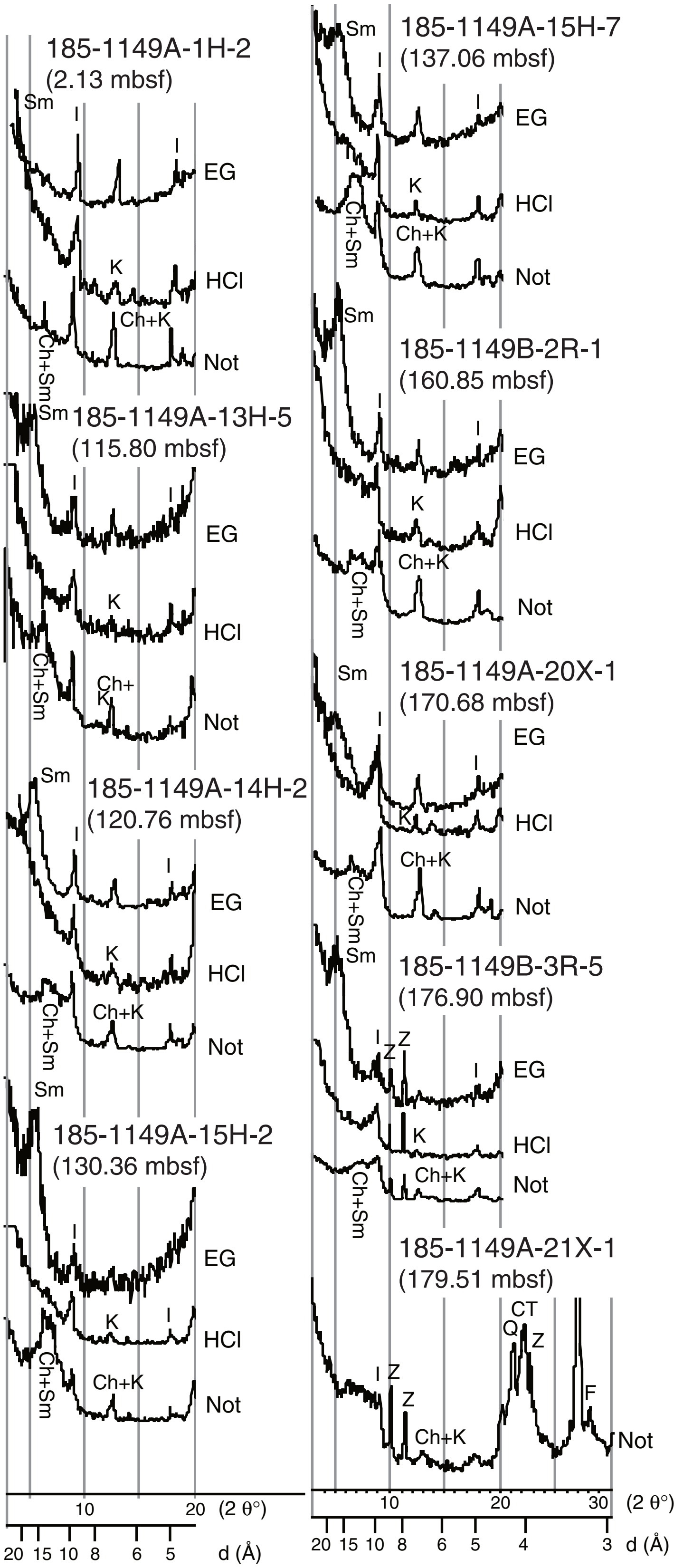

Figure F7. Ratio of clay mineral composition (smectite:illite:chlorite:kaolinite) in Units I and II.

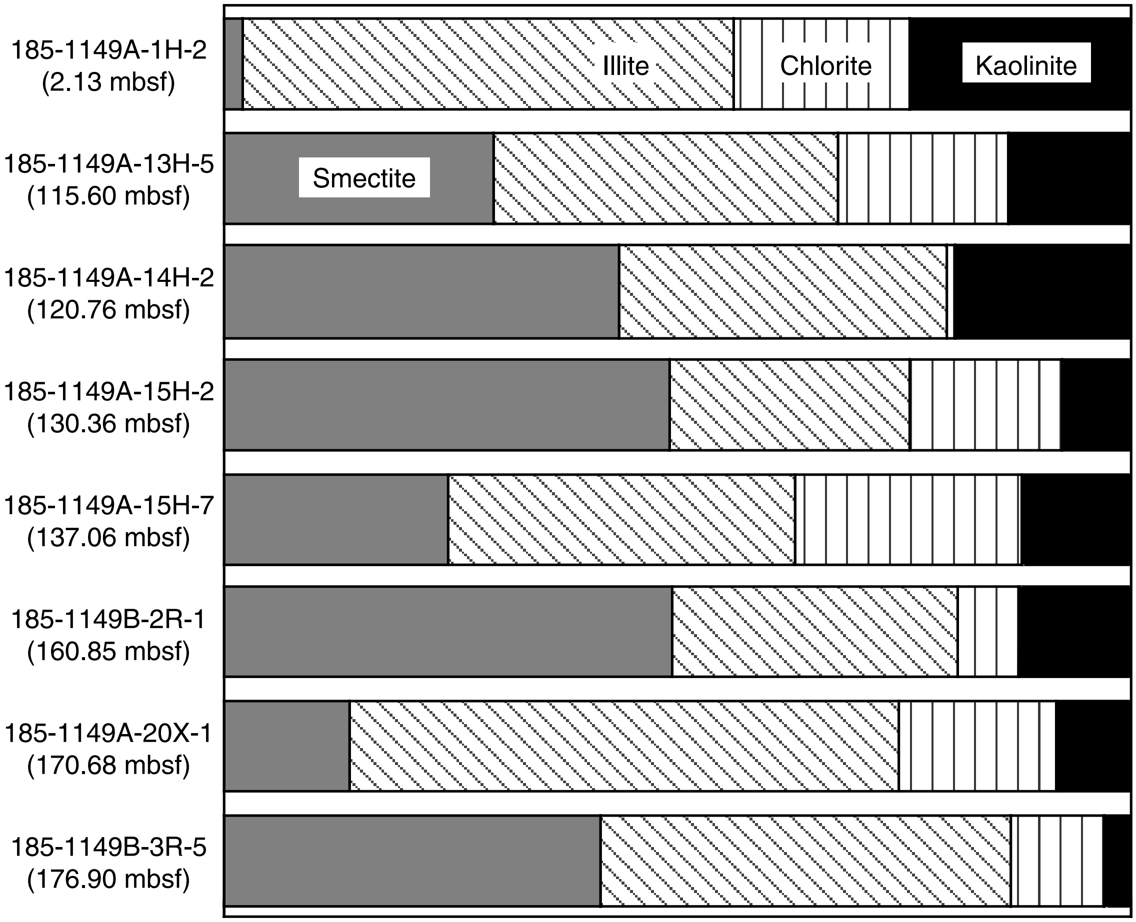

Figure F8. Microfabrics of Unit I. **A.** General view showing random and porous fabric from core at 2.13 mbsf (Sample 185-1149A-1H-2, 63–65 cm); vertical view, secondary electron image. **B.** Microfabrics from core at 52.49 mbsf (Sample 185-1149A-7H-1, 79–81 cm) showing random and porous fabric; vertical view, secondary electron image. **C.** Cross section from core at 2.13 mbsf (Sample 185-1149A-1H-2, 63–65 cm). Radiolarian tests in burrow are filled by fine sediments; vertical view, open nicols. **D.** Cross section from core at 115.60 mbsf (Sample 185-1149A-13H-5, 90–92 cm). Peds and macropores are seen in microfabric; vertical view, open nicols.

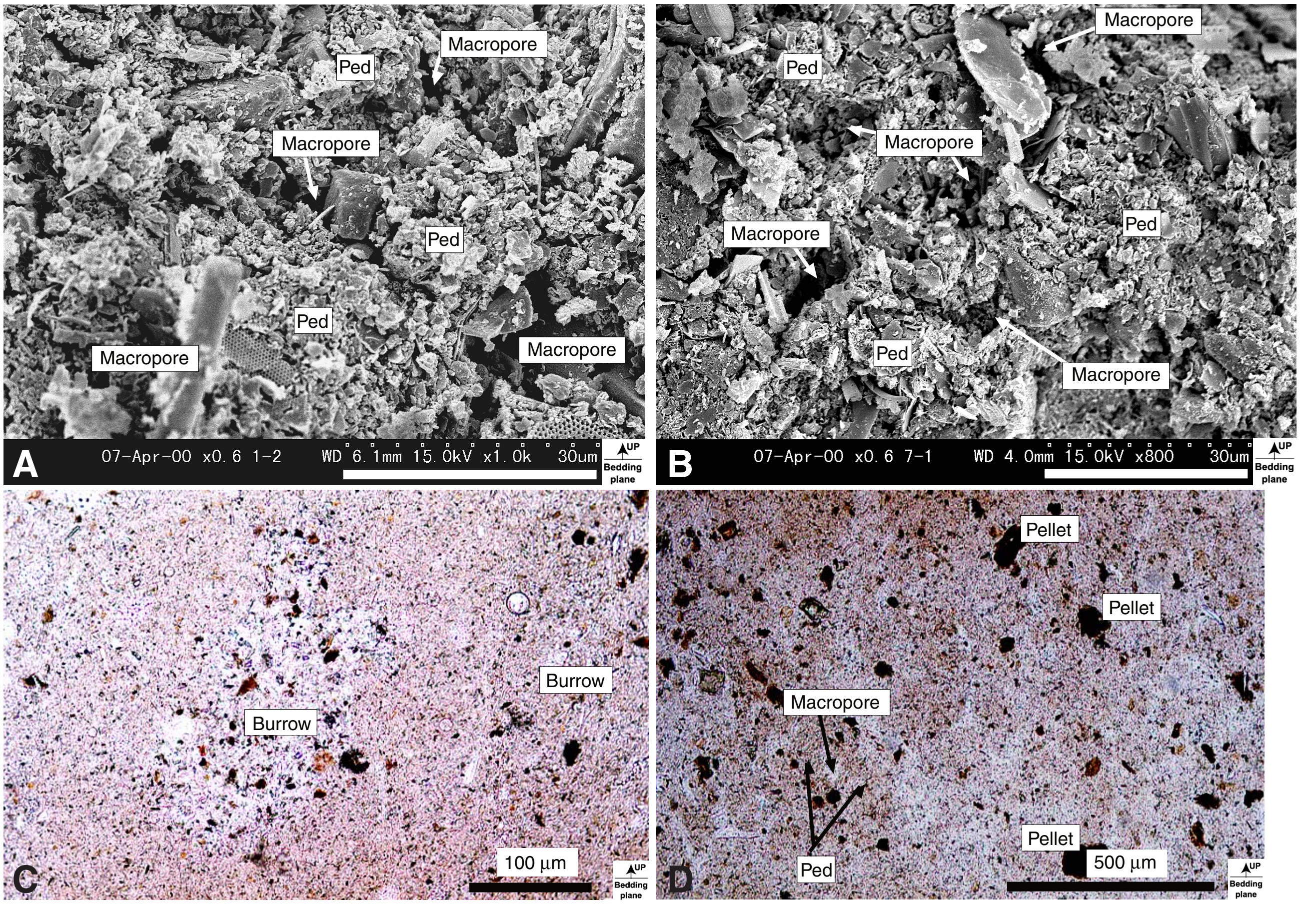

Figure F9. Microfabrics of Subunit IIA. **A.** General view showing random and porous fabric from core at 125.30 mbsf (Sample 185-1149A-14H-5, 110–112 cm); vertical view, secondary electron image. **B.** Close-up image of center of A. Peds are linked by clay platelets in EF contacts; vertical view, secondary electron image. **C.** Connectors, which are chain linked by each clay platelet in EF contact, at 125.30 mbsf (Sample 185-1149A-14H-5, 110–112 cm); vertical view, secondary electron image. **D.** Fabric showing preferred orientation of clay platelets from core at 125.30 mbsf (Sample 185-1149A-14H-5, 110–112 cm); vertical view, crossed nicols.

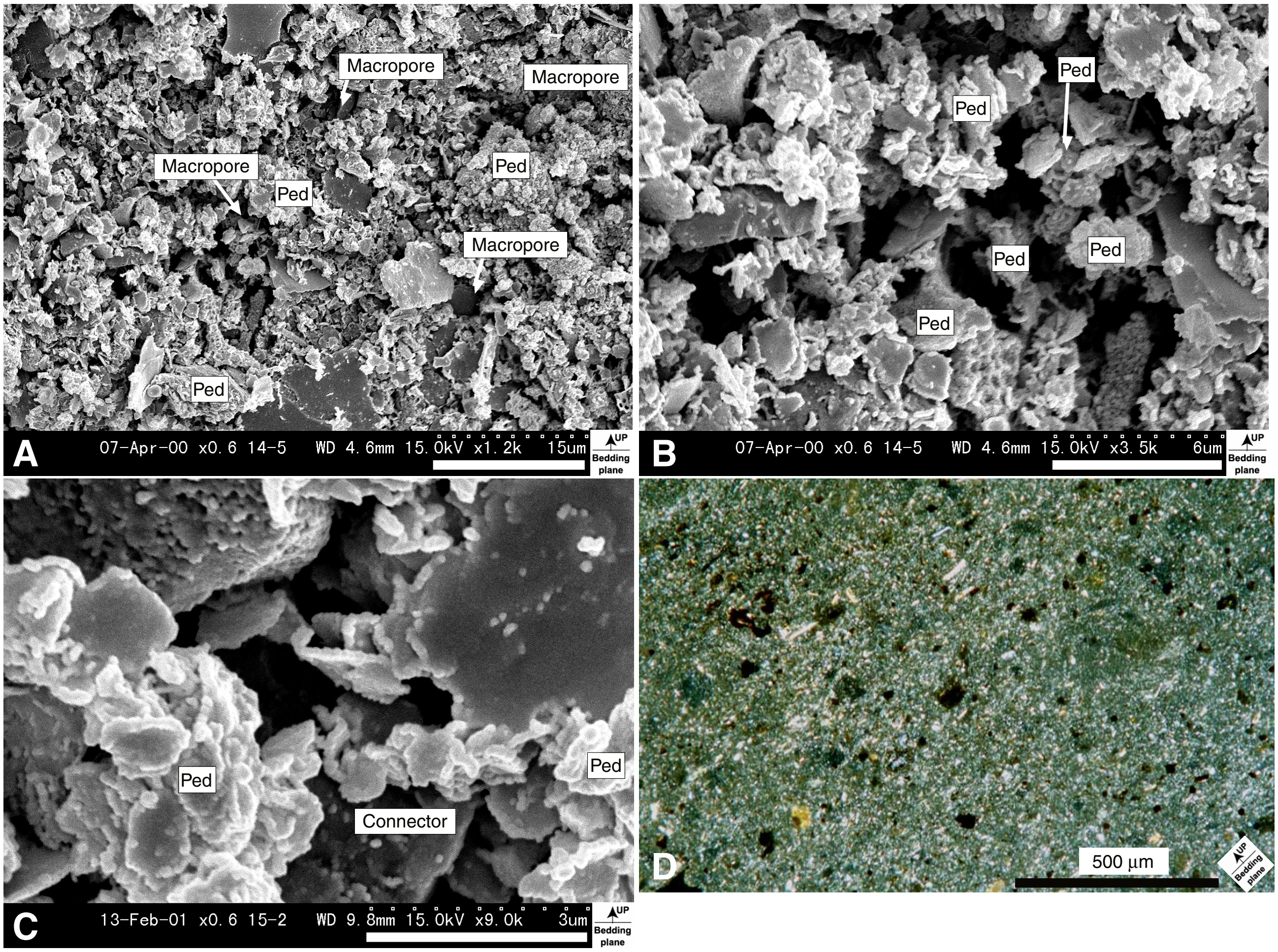

Figure F10. Microfabrics of Subunit IIB. **A.** General view showing random fabric of clay platelets in FF contact from core at 150.47 mbsf (Sample 185-1149A-17H-3, 77–79 cm); vertical view, secondary electron image. **B.** Fabric showing strongly preferred orientation of coarse-grained particles from core at 170.68 mbsf (Sample 185-1149A-20X-1, 88–90 cm); vertical view, secondary electron image. **C.** Close-up image of center of B; vertical view, secondary electron image. **D.** Fabric showing strongly preferred orientation of coarse-grained particles from core at 164.8 mbsf (Sample 185-1149A-19X-1, 40–42 cm). Note pressure solution around molding of radiolarian tests; vertical view, crossed nicols.

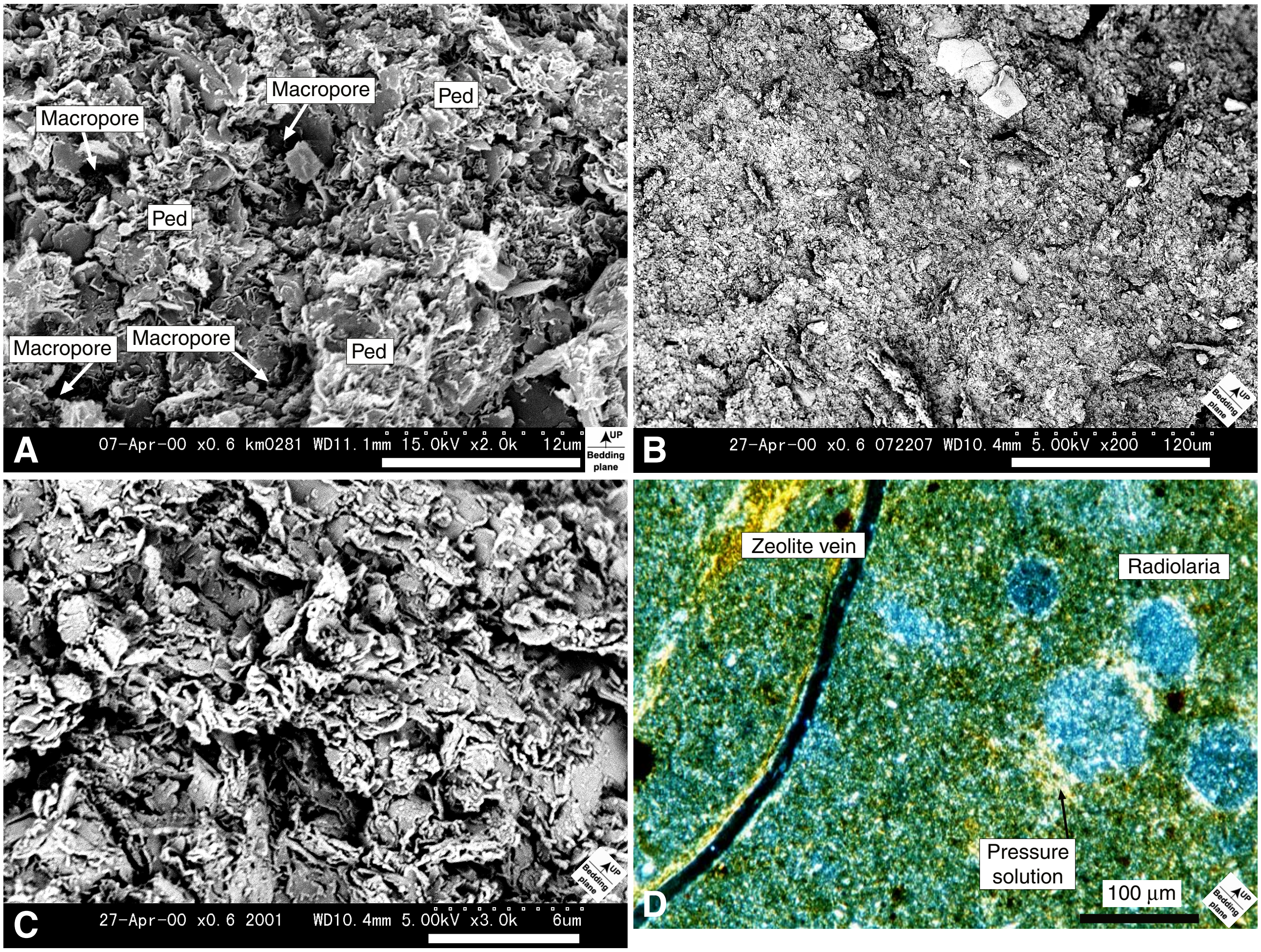

Figure F11. Palynomorphs, vertical views. **A, B, C.** Back-scatter images at 179.51 mbsf (Sample 185-1149A-21X-1, 41–43 cm). **D.** Secondary electron image at 170.68 mbsf (Sample 185-1149A-20X-1, 88–90 cm) that allows the upper direction to be shown.

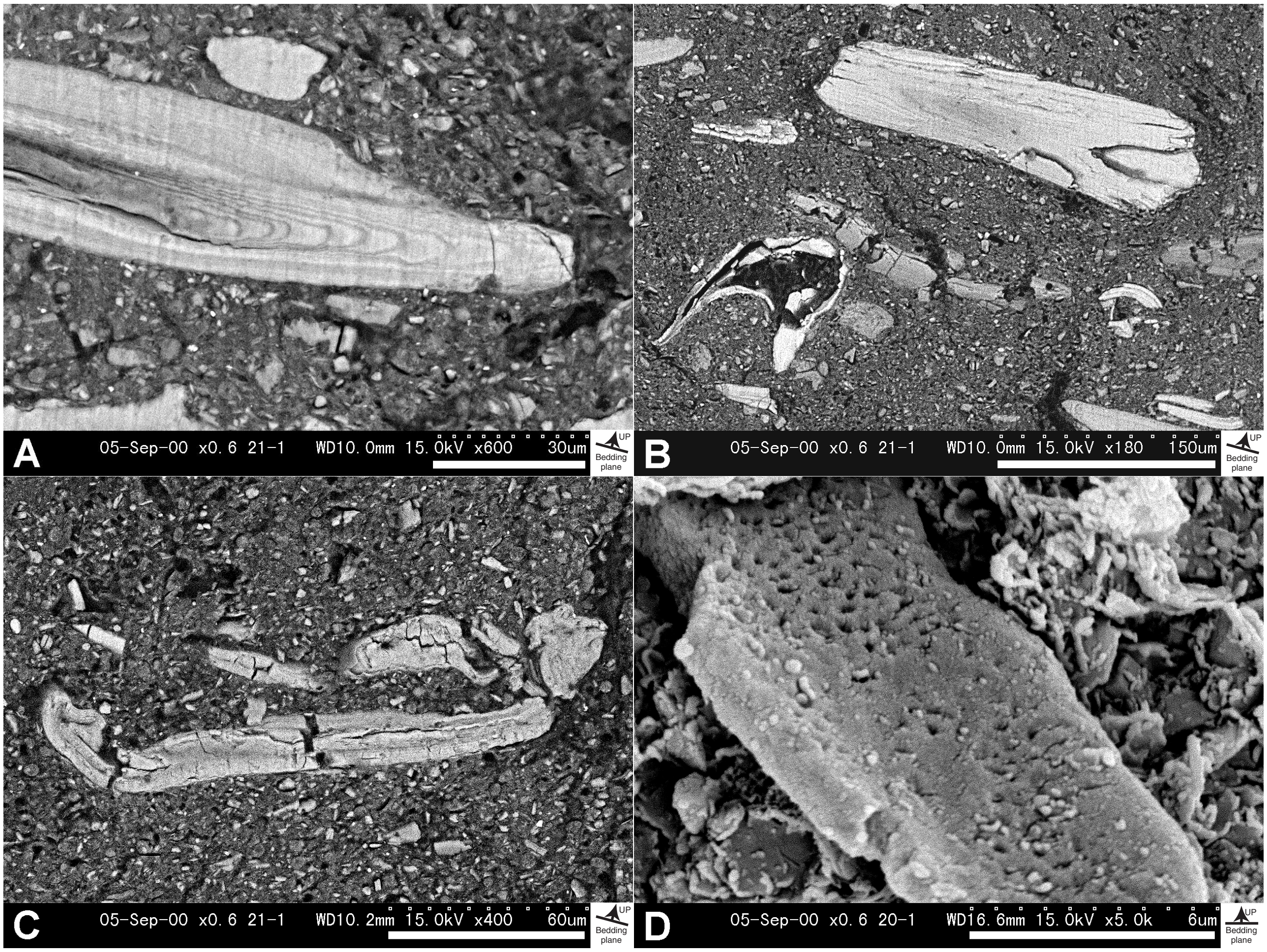

Figure F12. Microfabrics of Subunit IIB at 179.51 mbsf (Sample 185-1149A-21X-1, 41–43 cm). **A.** General view showing zeolite veins and faults. Zeolite veins are conjugated. **B.** Close-up view of zeolite vein. Microclinoptilolite grains in platy shape are seen in the vein. **C.** Detailed microfabric in zeolite vein observed by secondary electron image. Platy clinoptilolite grains are seen.

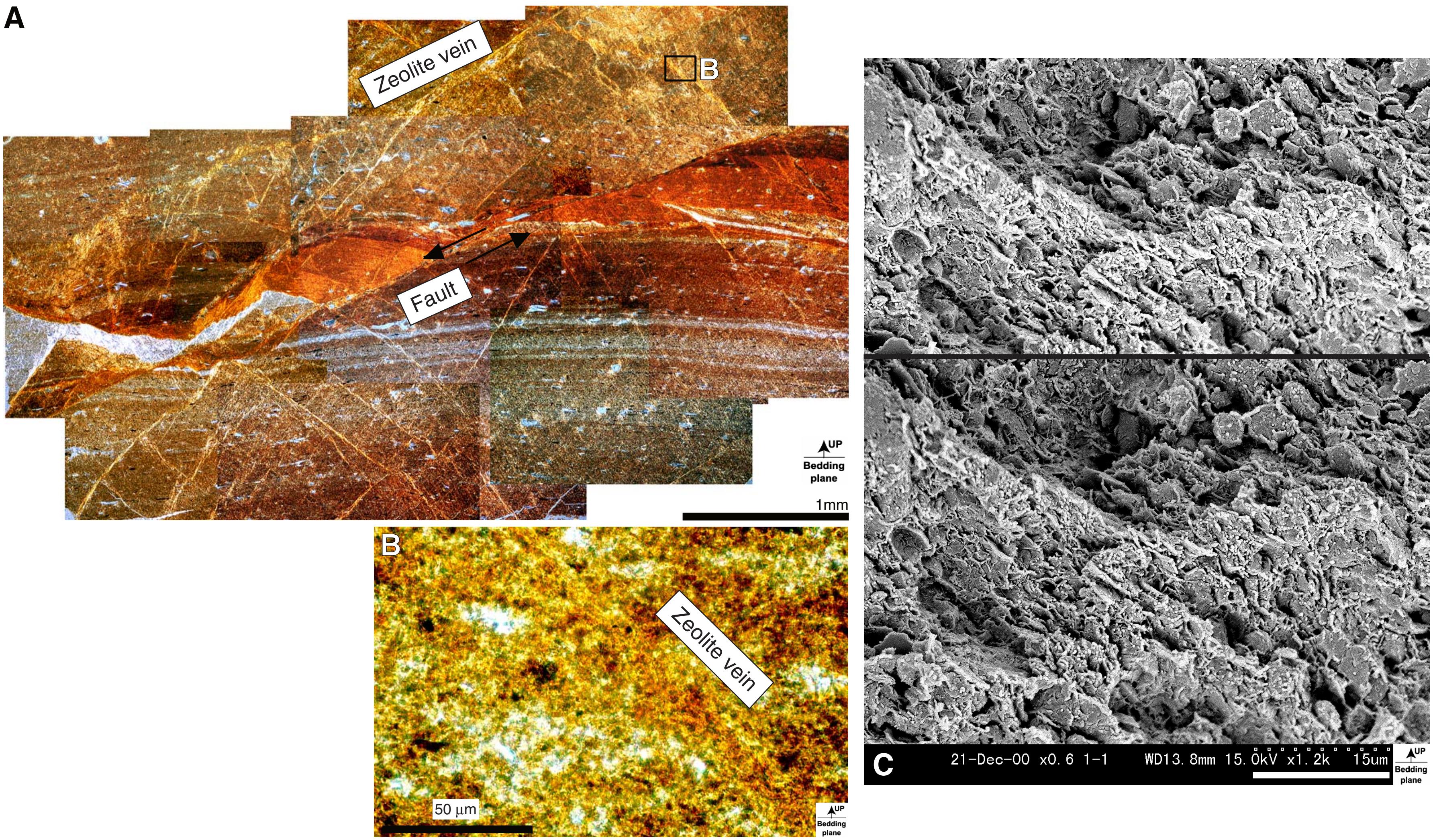

Figure F13. Schematic model of microfabrics in Unit I and Units IIA and IIB.

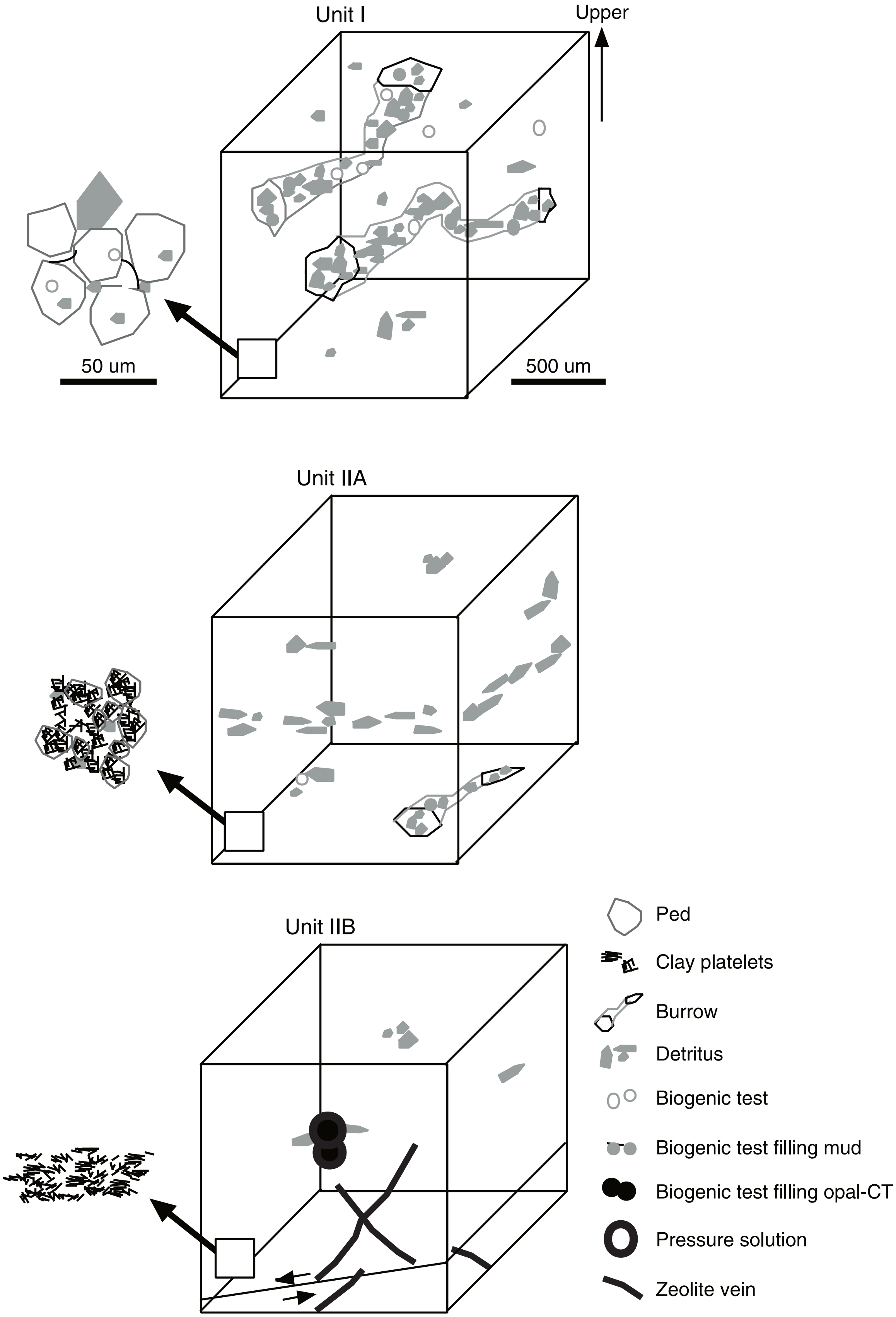

Table T1. Physical properties in Subunit IIB, Site 1149A.

Core, section, interval (cm)	Depth (mbsf)	Water content (dry%)	Wet bulk density (g/cm^3)	Porosity (%)	Void ratio
185-1149A-					
17H-3, 73–75	150.43	73.61	1.56	66.25	1.96
17H-4, 104–106	152.04	72.12	1.60	65.08	1.86
17H-5, 21–23	152.71	66.11	1.66	62.47	1.66
17H-6, 99–101	154.24	83.49	1.57	67.86	2.11
17H-7, 70–72	155.45	78.89	1.59	66.62	2.00
18H-1, 69–71	156.89	85.53	1.54	68.82	2.21
18H-2, 70–72	158.40	80.51	1.56	67.54	2.08
18H-3, 70–72	159.90	70.36	1.59	64.94	1.85
18H-4, 70–72	161.40	53.61	1.70	58.43	1.41
18H-5, 70–72	162.90	56.74	1.70	59.26	1.45
18H-6, 38–40	164.08	55.04	1.70	58.82	1.43
19X-1, 33–35	164.73	66.11	1.51	65.86	1.93
20X-1, 82–84	170.62	68.35	1.59	64.53	1.82
21X-1, 45–47	179.55	84.16	1.42	71.04	2.45

Notes: Water content and wet bulk density are data from onboard MST measurement. Porosity and void ratio are calculated by grain density 2.6 = g/cm^3.

Table T2. Magnetic susceptibility (MS) and anisotropy of MS data, Hole 1149A.

Core, section, interval (cm)	Depth (mbsf)	MS (10^{-3} SI)	P'	L	F	K_{max} Dec (°)	K_{max} Inc (°)	K_{min} Dec (°)	K_{min} Inc (°)
185-1149A-									
1H-2, 63–65	2.13	1.14	1.01	1.002	1.007	332.1	12.8	93.7	66.5
1H-3 37–39	3.37	0.81	1.006	1.001	1.004	69.21	14.6	285.31	72.2
3H-4, 37–39	9.07	0.67	1.014	1.006	1.008	298.05	1.8	142.45	88
2H-6, 53–55	12.23	0.55	1.017	1.002	1.013	153.66	13.1	357.96	75.6
3H-3, 88–90	17.58	0.75	1.006	1.004	1.002	163.62	8.7	62.92	50.5
4H-4, 131–133	29.01	0.81	1.008	1	1.007	188.64	1.5	288.34	81
5H-2, 110–112	35.30	0.95	1.009	1.005	1.004	136.55	15.8	243.35	45.6
6H-4, 62–64	47.32	0.82	1.011	1.004	1.007	287.89	13.2	18.99	4.8
6H-6, 30–32	50.00	0.76	1.016	1.004	1.012	69.19	67.4	305.09	13.1
7H-1, 79–81	52.49	0.97	1.004	1.002	1.001	300	49	188.5	17.7
7H-4, 15–17	56.35	0.74	1.01	1.004	1.007	44.6	29.1	312.9	3.1
8H-2, 108–110	63.78	0.89	1.008	1.005	1.003	218.94	14.3	330.34	55.1
8H-5, 42–44	67.62	0.64	1.011	1.007	1.004	138.48	9.2	286.58	79.2
9H-2, 51–53	72.71	1.15	1.013	1.004	1.008	41.77	2.1	137.87	70.8
9H-5, 88–90	77.58	0.95	1.011	1.005	1.006	1.06	5.5	220.56	82.8
10H-3, 57–59	83.77	1.12	1.007	1.004	1.003	220.84	21.6	120.94	23.5
10H-6, 65–67	88.35	0.62	1.007	1.003	1.004	72.55	14.6	193.65	63.2
11H-3, 73–75	93.43	0.82	1.015	1.007	1.008	210.09	24.6	75.29	57
11H-6, 48–50	97.68	0.92	1.004	1.001	1.003	175.35	11.9	303.05	70.9
12H-2, 60–62	101.30	0.61	1.004	1.002	1.002	327.78	5.3	222.68	70.3
12H-5, 76–78	106.01	0.64	1.008	1.004	1.003	98.34	7.2	250.94	81.9
13H-2, 81–83	111.01	0.71	1.005	1	1.004	26.37	5.9	250.47	81.8
13H-5, 90–92	115.60	1.19	1.001	1.001	1	142.56	3.1	33.66	80.5
14H-2, 106–108	120.76	1.72	1.016	1.003	1.011	301.01	2.9	96.41	86.8
14H-5, 110–112	125.30	0.86	1.028	1.001	1.024	231.78	16.3	76.18	72.2
15H-2, 116–118	130.36	2.06	1.057	1.002	1.048	303.62	8.3	164.62	79
15H-7, 36–38	137.06	2.02	1.065	1.005	1.053	7.46	0.9	214.06	89
16H-4, 88–90	142.58	1.41	1.058	1.003	1.048	239.69	0.2	145.69	86.8
17H-1, 85–87	147.55	0.86	1.052	1.001	1.044	141.13	1.8	40.03	80.7
18H-2, 65–67	158.35	1.01	1.033	1.001	1.029	250.75	3.3	138.55	81.2
18H-4, 75–77	161.45	0.59	1.038	1.002	1.031	325.24	8.6	197.44	76.2
19X-1, 40–42	164.80	0.86	1.061	1.001	1.052	338.38	6.2	232.48	68.3
20X-1, 88–90	170.68	1.37	1.066	1.001	1.056	107.84	4	213.84	75.6
185-1149B-									
2R-1, 25–27	160.85	0.64	1.028	1.017	1.01		43.1		39.9
3R-2, 65–67	172.45	1.52	1.017	1.001	1.014		5.9		69.9
3R-5, 60–62	176.90	1.49	1.003	1.002	1.002		12.3		33.3

Note: Dec = declination (°), Inc = inclination (°).